

Delineating white matter structure in diffusion tensor MRI with anisotropy creases

Gordon Kindlmann^{a,*}, Xavier Tricoche^b, Carl-Fredrik Westin^a

^a *Laboratory of Mathematics in Imaging, Department of Radiology, Harvard Medical School, USA*

^b *Computer Science Department, Purdue University, USA*

Received 2 May 2007; received in revised form 16 July 2007; accepted 17 July 2007

Available online 3 August 2007

Abstract

Geometric models of white matter architecture play an increasing role in neuroscientific applications of diffusion tensor imaging, and the most popular method for building them is fiber tractography. For some analysis tasks, however, a compelling alternative may be found in the first and second derivatives of diffusion anisotropy. We extend to tensor fields the notion from classical computer vision of ridges and valleys, and define *anisotropy creases* as features of locally extremal tensor anisotropy. Mathematically, these are the loci where the gradient of anisotropy is orthogonal to one or more eigenvectors of its Hessian. We propose that anisotropy creases provide a basis for extracting a skeleton of the major white matter pathways, in that ridges of anisotropy coincide with interiors of fiber tracts, and valleys of anisotropy coincide with the interfaces between adjacent but distinctly oriented tracts. The crease extraction algorithm we present generates high-quality polygonal models of crease surfaces, which are further simplified by connected-component analysis. We demonstrate anisotropy creases on measured diffusion MRI data, and visualize them in combination with tractography to confirm their anatomic relevance.

© 2007 Elsevier B.V. All rights reserved.

Keywords: Diffusion tensor MRI; Anisotropy; Ridges and valleys; Crease surface extraction; White matter geometry

1. Introduction

Diffusion tensor magnetic resonance imaging (DTI) has become a popular means of measuring the structure of white matter in the central nervous system (Basser et al., 1994; Pierpaoli et al., 1996; Basser and Jones, 2002). The coherent organization of axons in nerve bundles contributes to the magnitude and orientation of diffusion anisotropy (Beaulieu, 2002). To the extent that a single diffusion tensor model captures the diffusive behavior in the underlying tissue, image processing of tensor-valued data can be leveraged to analyze the macroscopic architecture of the white matter in disease and in health. The de facto standard measure of microstructural tissue organization, calculated from the diffusion tensor, is *fractional anisotropy*, or

FA (Basser, 1995). Many applications of DTI are based on region-of-interest measurements of FA, guided either by prior knowledge of neuroanatomy, or by measurements from functional MRI (Klingberg et al., 2000; Kubicki et al., 2003; Kanaan et al., 2005; Salat et al., 2005; Tuch et al., 2005).

Fiber tractography is another common DTI analysis method, in which the course of axons in fiber tracts is approximated by path integrals along the direction of greatest diffusivity, the diffusion tensor principal eigenvector (Basser et al., 2000). Neuroscientific studies can then be based upon measurements of tract geometry (Dougherty et al., 2005) or of tensor attributes along tracts (Corouge et al., 2006). Further post-processing of tractography can involve *clustering* coherent groups of similar tracts into models of major fiber pathways (Zhang et al., 2006; O'Donnell et al., 2006). The combination of tractography and clustering algorithms requires a non-trivial number of parameter settings, which may affect their practical

* Corresponding author. Tel.: +1 617 525 6074; fax: +1 617 582 6033.
E-mail address: gk@bwh.harvard.edu (G. Kindlmann).

application to neuroscientific studies (Moberts et al., 2005). This has motivated our exploration of modeling techniques that work more directly with the underlying tensor data and its attributes.

In two-dimensional images and height fields, ridges and valleys, collectively referred to as *creases*, have been an object of study for many years in different disciplines. In the context of geomorphology, de Saint-Venant (1852) defines creases as the loci where the slope is minimal along the isocontours of the relief, which was later reformulated in terms of the Hessian of the height function by Haralick (1983). Maxwell (1870) gives a topological and global definition of ridges and valleys as watersheds and watercourses: slope lines that connect saddle points to local maxima or minima. Gauch and Pizer (1993) define ridges in terms of differential geometry and topography, and track them through multiple scales of image feature size. More generally, the localization of ridge and edge features in both position and intrinsic scale is a focus of extensive research (see e.g. Lindeberg, 1998 or ter Haar Romeny, 2003 and references therein). Most relevant for our approach, Eberly et al. (1994) motivate the idea that creases should be defined locally and be invariant with respect to a variety of transforms (rigid transforms, uniform scaling, and monotonic mappings of intensity), and they generalize the height-based definition of de Saint-Venant to d -dimensional manifolds embedded in n -dimensional image space. Other previous work focuses on extracting polygonal models of crease geometry; this is reviewed in Section 3.1.

We propose that a skeleton of the major white matter structures can be approximated from creases extracted directly from the differential properties of scalar-valued tensor attributes. Given the ubiquity of FA as a quantitative variable in the diffusion tensor literature, we start by detecting creases in FA, and term these *anisotropy creases* (Kindlmann et al., 2006). We propose that the ridge surfaces and ridge lines of FA coincide with the interiors of white matter fiber tracts, and that valley surfaces of anisotropy delineate the interfaces between fiber tracts that are adjacent but distinctly oriented (such as between the corpus callosum and the cingulum bundles). Anisotropy creases may have utility in a variety of contexts, such as non-rigid registration and shape analysis. The ability to extract white matter skeletons directly from tensor invariants, without the algorithmic complexity or parameter tuning of fiber tracking and clustering, could also increase sensitivity in shape analysis studies. We emphasize that our algorithm is fundamentally a local *structural* analysis of tensor image features, rather than a global *connectivity* analysis. That is, we seek geometric models of major white matter structures and their interfaces, not a detailed connectivity model over the entire brain.

Major crease features may also play a role analogous to that of the cortical surface in functional imaging, that is, a reference manifold onto which variables of interest are projected and analyzed. This general strategy is advanced

by the tract-based spatial statistics (TBSS) method of Smith et al. (2006) (see Rouw and Scholte, 2007 for an example application). TBSS enables voxel-based morphometry on a white matter skeleton calculated from ridges in a smooth mean FA image (from a set of registered scan), although “ridges” are not mentioned per se, and the ridge representation is a discrete raster image. By using an established mathematical definition of crease features, our technique extracts true codimension-one crease surfaces from continuous tensor fields, from individual DTI scans. Other examples of previous work in feature detection in DTI have also used, as we do, derivatives in tensor fields rather than tractography. Pajevic et al. (2002) use B-splines to generate continuous tensor fields that are differentiated to highlight anisotropy boundaries. O’Donnell et al. (2004) use structure tensors to detect general boundaries in tensor values. In both cases, results are visually evaluated by confirming a high edge strength near structural boundaries, but the techniques do not analyze the familiar FA measure, nor is the feature geometry explicitly extracted.

2. Theoretical background

2.1. Fractional anisotropy and its derivatives

Our method is based on measuring the differential structure of fractional anisotropy (FA), so we review here the definition of FA (which leads to formulae for its spatial derivatives) and a method of creating a second-order continuous tensor field from sampled data. We notate the tensor trace and determinant as $\text{tr}()$ and $\det()$, respectively, the identity tensor as \mathbf{I} , and the tensor norm as

$|\mathbf{D}| = \sqrt{\text{tr}(\mathbf{D}\mathbf{D}^T)}$. The eigenvalues λ_i of tensor \mathbf{D} are the roots of the characteristic polynomial $p(\lambda) = \det \lambda \mathbf{I} - \mathbf{D}$, and the coefficients of $p(\lambda)$ are the principal invariants J_1, J_2, J_3 (Bourne and Kendall, 1977). An additional invariant J_4 can be defined for convenience:

$$\begin{aligned} J_1 &= \text{tr}(\mathbf{D}); & J_2 &= \frac{\text{tr}(\mathbf{D})^2 - \text{tr}(\mathbf{D}^2)}{2}; \\ J_3 &= \det(\mathbf{D}); & J_4 &= |\mathbf{D}|^2. \end{aligned} \quad (1)$$

Basser and Pierpaoli (1996) define FA in terms of the deviatoric tensor $\tilde{\mathbf{D}} = \mathbf{D} - \text{tr}(\mathbf{D})\mathbf{I}/3$ and tensor contraction $\mathbf{A}:\mathbf{B} = \text{tr}(\mathbf{A}\mathbf{B}^T)$, which with some algebra can be re-expressed in terms of J_2 and J_4 :

$$\text{FA} = \sqrt{\frac{3}{2} \frac{\tilde{\mathbf{D}}:\tilde{\mathbf{D}}}{\mathbf{D}:\mathbf{D}}} = \sqrt{1 - J_2/J_4}. \quad (2)$$

J_2 and J_4 can in turn be expressed in terms of the individual tensor coefficients:

$$J_2 = D_{xx}D_{yy} + D_{xx}D_{zz} + D_{yy}D_{zz} - D_{xy}^2 - D_{xz}^2 - D_{yz}^2 \quad (3)$$

$$J_4 = D_{xx}^2 + D_{yy}^2 + D_{zz}^2 + 2D_{xy}^2 + 2D_{xz}^2 + 2D_{yz}^2 \quad (4)$$

Applying the chain rule to Eq. (2) generates an expression for the spatial gradient of FA in terms of the spatial gradients of the individual tensor components:

$$\nabla \text{FA} = \frac{J_2 \nabla J_4 - J_4 \nabla J_2}{2J_4^2 \text{FA}} \quad (5)$$

$$\begin{aligned} \nabla J_2 = & (D_{yy} + D_{zz}) \nabla D_{xx} + (D_{xx} + D_{zz}) \nabla D_{yy} \\ & + (D_{xx} + D_{yy}) \nabla D_{zz} - 2(D_{xy} \nabla D_{xy} + D_{xz} \nabla D_{xz} \\ & + D_{yz} \nabla D_{yz}) \end{aligned} \quad (6)$$

$$\begin{aligned} \nabla J_4 = & 2(D_{xx} \nabla D_{xx} + D_{yy} \nabla D_{yy} + D_{zz} \nabla D_{zz}) \\ & + 4(D_{xy} \nabla D_{xy} + D_{xz} \nabla D_{xz} + D_{yz} \nabla D_{yz}) \end{aligned} \quad (7)$$

The formula for the second derivative (the Hessian) of FA is given in [Appendix A](#). Our formulaic decomposition of the derivatives of FA also translates to an implementation strategy, in which J_2 , J_4 and their spatial derivatives are numerically computed (as described in the next section), and then combined to find the gradient and Hessian of FA.

2.2. Continuous field reconstruction

Our method of crease extraction relies on a second-order continuous (C^2) reconstruction of the tensor field from the discretely sampled data. Previous work has advanced the use of cubic B-splines for interpolating the sampled tensor coefficients to create a C^2 tensor field ([Aldroubi and Basser, 1999](#); [Pajevic et al., 2002](#)). The geometric structure of the crease features, however, does not depend on exact interpolation of the tensor values, and for the purposes of robust-

ness with respect to sample noise it is advantageous for some amount of blurring to be incorporated into the field reconstruction. More generally, techniques in computer vision for localizing image features in scale-space typically use Gaussian blurring to low-pass filter the image data ([Lindeberg, 1998](#); [ter Haar Romeny, 2003](#)).

We have as yet not pursued a full scale-space extraction of anisotropy creases, but we have used Gaussian blurring at a fixed scale as a pre-process (details in [Section 4](#)), followed by separable reconstruction with the uniform cubic B-spline function $b(x)$ as a (non-interpolating) C^2 kernel.

$$b(x) = \begin{cases} 0 & |x| > 2 \\ -(|x| - 2)^3/6 & 1 < |x| < 2 \\ (|x| - 2)|x|^2/2 + 2/3 & 0 < |x| < 1 \end{cases} \quad (8)$$

By linearity of convolution-based reconstruction and differentiation, analytic derivatives of the reconstructed field are measured by convolving the sampled data with derivatives of the reconstruction kernel ([Gonzalez and Woods, 2002](#)). The partial derivatives of the separable three-dimensional reconstruction kernel $B(x, y, z) = b(x)b(y)b(z)$ can be determined by, for example, $\partial B/\partial x = b'(x)b(y)b(z)$. The uniform cubic B-spline kernel $b(x)$ does not “ring” or add additional extrema in the reconstructed function, which in our experience has avoided the creation of false crease responses around tissue boundaries.

As should be clear from Eq. (2), FA is a non-linear function of the tensor: $\text{FA}(\mathbf{A} + \mathbf{B}) \neq \text{FA}(\mathbf{A}) + \text{FA}(\mathbf{B})$. This has bearing on how FA and its spatial derivatives are com-

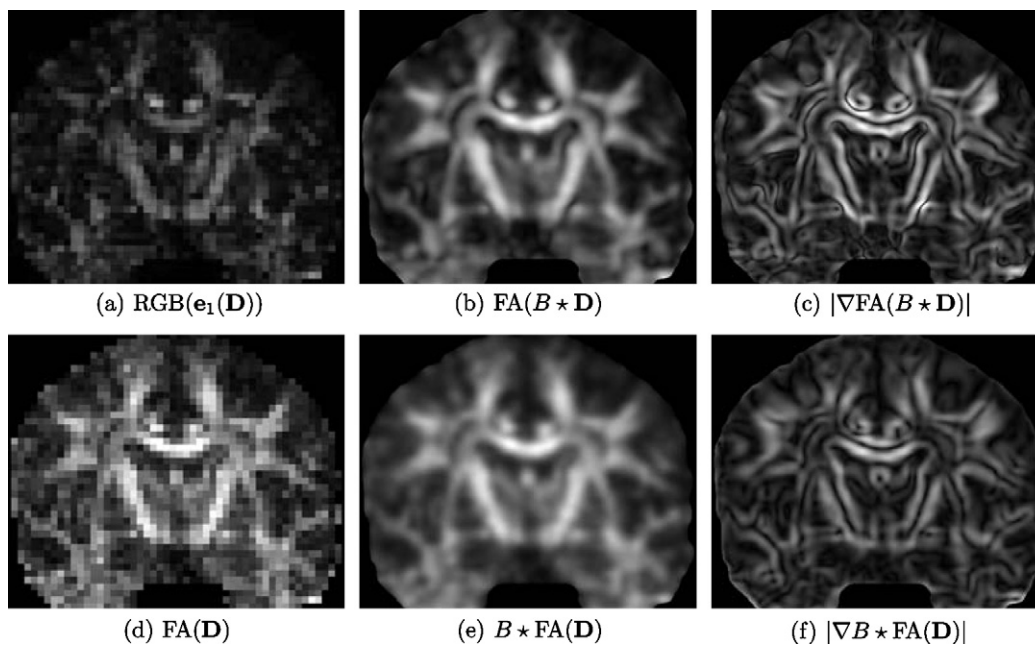


Fig. 1. FA calculation does not commute with convolution-based reconstruction or differentiation. A slice of sampled tensor data \mathbf{D} is shown with the standard RGB color map (a) ([Pajevic and Pierpaoli, 1999](#)) or FA map (d). Convolving the discrete tensor data with a continuous reconstruction kernel B produces a continuous tensor field, in which we measure FA (b) and $|\nabla \text{FA}|$ (c). Convolving the discrete FA data $\text{FA}(\mathbf{D})$ with B gives a continuous FA field (e) and $|\nabla \text{FA}|$ (f). Note that the shape and boundaries of the finer structures in (b) appear blurred in (e), especially near the center of the image. This is confirmed by the $|\nabla \text{FA}|$ images; interfaces between major tracts visible in (a) remain sharp in (c) but indistinct in (f).

puted from discretely sampled tensor data. Specifically, pre-computing FA on a discrete grid and then convolving or differentiating (an approach taken by, for example, Goodlett et al., 2006) is not equivalent to analytically calculating the FA and its derivatives (by Eq. (5)) of a continuous tensor field reconstruction. Fig. 1 demonstrates this with a two-dimensional coronal slice of a human brain DTI scan (acquisition details given in Section 4). One of the contributions of our approach is incorporating the analytic calculation of FA (and its derivatives) directly into the crease-finding algorithm, rather than the more straight-forward approach of pre-computing a scalar FA field and then applying an existing crease-finding method.

2.3. Crease feature definition

Eberly et al. (1994) define crease features of a scalar field f in terms of the gradient $\mathbf{g} = \nabla f$ and Hessian \mathbf{H} , in a way that easily generalizes to three and higher-dimensional images. Intuitively, creases are loci of constrained extrema, with the constraint surface defined by tangency to one or more Hessian eigenvectors. A function is at extrema where its gradient is orthogonal to the constraint surface (Marsden and Tromba, 1996), so in three dimensions ridges and valleys occur where the gradient \mathbf{g} is orthogonal to one or two of the unit-length eigenvectors $\{\mathbf{e}_1, \mathbf{e}_2, \mathbf{e}_3\}$ (with corresponding sorted eigenvalues $\lambda_1 \geq \lambda_2 \geq \lambda_3$) of the Hessian \mathbf{H} :

	Surface	Line
Ridge	$\mathbf{g} \cdot \mathbf{e}_3 = 0, \lambda_3 < 0$	$\mathbf{g} \cdot \mathbf{e}_2 = \mathbf{g} \cdot \mathbf{e}_3 = 0, \lambda_3, \lambda_2 < 0$
Valley	$\mathbf{g} \cdot \mathbf{e}_1 = 0, \lambda_1 > 0$	$\mathbf{g} \cdot \mathbf{e}_1 = \mathbf{g} \cdot \mathbf{e}_2 = 0, \lambda_1, \lambda_2 > 0$

In this definition, the strength of the image feature can be assessed by the magnitude of the eigenvalues that are required to be negative or positive for ridges and valleys, respectively, which can be used to filter out insignificant features. Specifically, crease surface strength is measured by $-\lambda_3$ (for ridges) and λ_1 (for valleys), and crease line strength is measured by $-\lambda_2$ (for ridges) and λ_2 (for valleys).

3. Methods

3.1. Crease surface extraction

In our work to date we have implemented geometric extraction of crease surfaces, but not crease lines, because surfaces constitute the majority of the fiber tract geometry that we seek to capture. We extract crease surfaces by per-voxel triangulation of the zero-isocontour of $\mathbf{g} \cdot \mathbf{e}_i$ ($\mathbf{g} \cdot \mathbf{e}_3$ for ridges, $\mathbf{g} \cdot \mathbf{e}_1$ for valleys) using marching cubes (MC) (Lorenson and Cline, 1987). Straight-forward application of MC, however, would not produce useful results, because the inherent sign ambiguity of eigenvectors leads to arbi-

trary signs in $\mathbf{g} \cdot \mathbf{e}_i$, which must be consistent for the MC case tables to apply. The literature offers ways to overcome this. Morse (1994) suggests determining correspondences between sets of eigenvectors rather than individual ones, to handle eigenvector permutations associated with eigenvalue equality. Furst et al. (1996) use similar ideas in *marching cores* to extract crease manifolds in image scale-space. In their *marching ridges* method, Furst and Pizer (2001) compute the principal eigenvector of the average of outer products of the eigenvectors at voxel corners, and use its (arbitrary) sign to impose a consistent sign to eigenvectors at voxel corners.

We have taken a more cautious approach, based on observations suggesting that eigenvectors of the Hessian of *non-linear* scalar attributes of *tensors* (such as FA) can vary more rapidly than Hessian eigenvectors of a similarly sampled *scalar* field, which may confound the heuristics (described above) developed for scalar fields. Thus, we determine the correspondence between eigenvector signs at the voxel corners by continuously tracking the eigenvector orientation along each voxel edge. Point samples are adaptively generated along all voxel edges until the angle between eigenvectors at adjacent samples are reduced below a threshold (20° in our current work). This process, which is currently the most time-consuming component of our approach, determines whether the smooth transport of $\mathbf{e}_i(\mathbf{v}_0)$ from vertex \mathbf{v}_0 to vertex \mathbf{v}_1 agrees in sign with eigenvector $\mathbf{e}_i(\mathbf{v}_1)$ or $-\mathbf{e}_i(\mathbf{v}_1)$ computed at \mathbf{v}_1 . The per-edge eigenvector sign information is propagated along all voxel edges to determine a per-voxel sign consistency prior to evaluating the MC case. This process ensures intra-voxel eigenvector sign consistency, but not inter-voxel sign consistency, which creates triangulations with inconsistent vertex windings (the clockwise versus counter-clockwise order in which the triangle's vertices are listed). Thus, as a final pass, we traverse the crease surface mesh to make the vertex windings consistent, while splitting the surface with vertex duplication in the case of non-orientable surfaces. This allows graphics hardware to appropriately render the crease surfaces with two-sided lighting (Shreiner et al., 2004).

The remaining details of our method can decrease the computation time and increase the utility of the results. We refer to the grid on which the crease surface is triangulated one voxel at a time (by our modified MC) as the *triangulation grid*. The continuous tensor field measurements (Section 2.2) allow the resolution of the triangulation grid to be independent of the sampling of underlying tensor data. A triangulation grid with finer sampling (higher resolution) than the underlying data improves the quality of the crease surface triangulation, yet no up-sampling to the triangulation grid is required as a pre-process. By sampling the crease surface strength (FA Hessian eigenvalue $-\lambda_3$ for ridges, λ_1 for valleys) at the vertices of triangulation grid, we can skip the voxels that are unlikely to contribute to the crease surface. Even with these pre-cautions, the extracted crease surfaces are often made of many disjoint

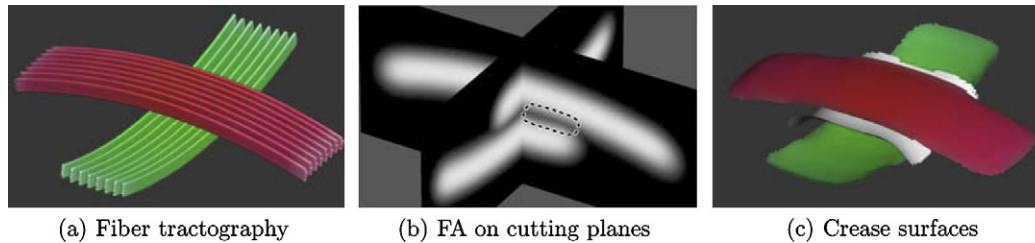


Fig. 2. Demonstration of FA ridge and valley surfaces in a synthetic dataset. The tractography of the two arcs in (a) is color-coded by the usual $\text{RGB}(\mathbf{e}_i)$. The lower FA between the arcs is highlighted in (b). In (c), the red and green ridge surfaces correctly model the shape of bands, and the white valley surface captures the interface between them. (For interpretation of the references to color in this figure legend, the reader is referred to the web version of this article.)

pieces. We use connected-component analysis on the polygonal crease surfaces to filter out all but the largest few of the crease surface components. We believe that removing the smallest components increases the anatomic significance of the crease surface results by removing the pieces that are most apt to vary as a function of image noise and scale selection. This geometric post-processing is a significant improvement over the method presented in our previous work (Kindlmann et al., 2006).

We demonstrate the method on a synthetic dataset prior to giving results on DTI scans. Fig. 2 shows results on a synthetic dataset containing two adjacent bands of orthogonally oriented linear anisotropy. The ridge surfaces of FA represent the interiors of the two bands, and the valley surface of FA marks the interface between them. It is in this sense that we claim that crease surfaces model the skeleton of the white matter fiber geometry.

4. Results

The results in this section used tensor data acquired on a 1.5 T Philips scanner with SENSE parallel imaging (reduction factor 2.5), using single-shot spin echo EPI diffusion-weighted images along 30 non-collinear gradient directions ($b = 700 \text{ s/mm}^2$), with five non-diffusion-weighted T2 images. The field of view, the size of the acquisition matrix, and the slice thickness were $240 \times 240 \text{ mm}$, 96×96 , and 2.5 mm , respectively, leading to an image resolution of 2.5 mm^2 . Fifty-five axial slices were acquired to cover the entire brain. Unless otherwise noted, the standard deviation σ of the Gaussian smoothing kernel (prior to B-spline-based reconstruction and differentiation) was 1.25 mm , and the resolution of the triangulation grid is five times that of the underlying tensor dataset. The computation timings are with a 1.67 GHz PowerPC G4 with 2 GB of memory.

4.1. Slice inspection

Prior to their geometric extraction, the numerical ingredients of anisotropy crease features can be visualized on densely sampled slices. Fig. 3 shows the numerical constituents of crease features on the same dataset slice used in

Fig. 1. The strength measures described in Section 2.3 are visualized in the top half of the figure. These are used to modulate the display in the bottom half of the figure of the scalar function whose zero level-set defines the crease feature, with some additional contrast enhancement for clarity. Crease surfaces intersect with the cutting plane in curves, and crease lines intersect with the plane in points. Note that the ridge surfaces (Fig. 3d) closely follow the shape of the major white matter tracts (annotated in Fig. 4a), and the valley surfaces (Fig. 3e) delineate the interface between tracts that are adjacent but distinctly oriented. The anatomic utility of the ridge lines (Fig. 3f) is limited to tracts with a more cylindrical shape, that is, features for which the two smallest eigenvalues λ_2 and λ_3 of the Hessian are approximately equal. This includes the cingulum bundles and fornix (Mori et al., 2005), although the non-zero response of $s_{r/l}$ through-out the slice complicates visual confirmation.

The renderings in Fig. 4 (from a posterior viewpoint) show a cropped region around the same coronal slice of previous figures. In Fig. 4a fibers are seeded from the RGB-encoded plane, and some of the major pathways are indicated. Fig. 4b shows how the ridge surfaces (using the same RGB encoding) follow major fiber paths, especially the corpus callosum (CC), internal capsule (IC), corona radiata (CR), and fornix (FX) (Mori et al., 2005). The (white) anisotropy valley surfaces in Fig. 4c delineate interfaces between the CC and cingulum bundles (CB), superior fronto-occipital fasciculus (SFO) and IC, and IC and superior longitudinal fasciculus (SLF). Fig. 4d also illustrates how anisotropy valleys lie between adjacent paths of differing orientation. The ridge and valley surface extractions each took 10 min.

Fig. 5 illustrates anisotropy crease analysis in the brainstem (lateral anterior superior viewpoint), a region with a closely contained complex of fiber pathways along distinct directions (Salamon et al., 2005). For anatomical context, Fig. 5a shows fiber tractography results, including the (from ventral to dorsal) middle cerebellar peduncle (MCP), corticospinal tract (CST), transverse pontine tract (TPT), medial lemniscus (ML), superior cerebellar peduncle (SCP), and inferior cerebellar peduncle (ICP). These pathways appear as anisotropy ridge surfaces in Fig. 5b.

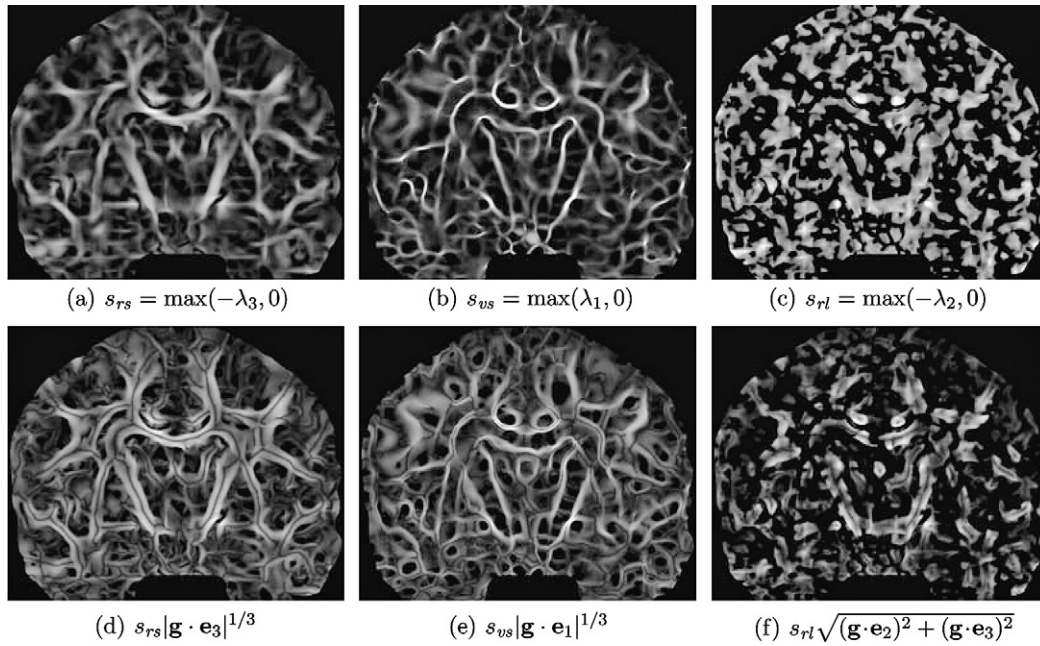


Fig. 3. Functional components of crease feature definition. The ridge surface strength s_{rs} (a), valley surface strength s_{vs} (b), and ridge line strength s_{rl} (c) are all defined in terms of the eigenvalues of the FA Hessian. These are used to modulate the display of the ridge surface (d), valley surface (e), and ridge line (f) functions defined in terms of the FA gradient \mathbf{g} and Hessian eigenvectors \mathbf{e}_i . The crease features are visible as dark lines (in the case of crease surfaces) or dark dots (in the case of ridge lines) in the bright areas.

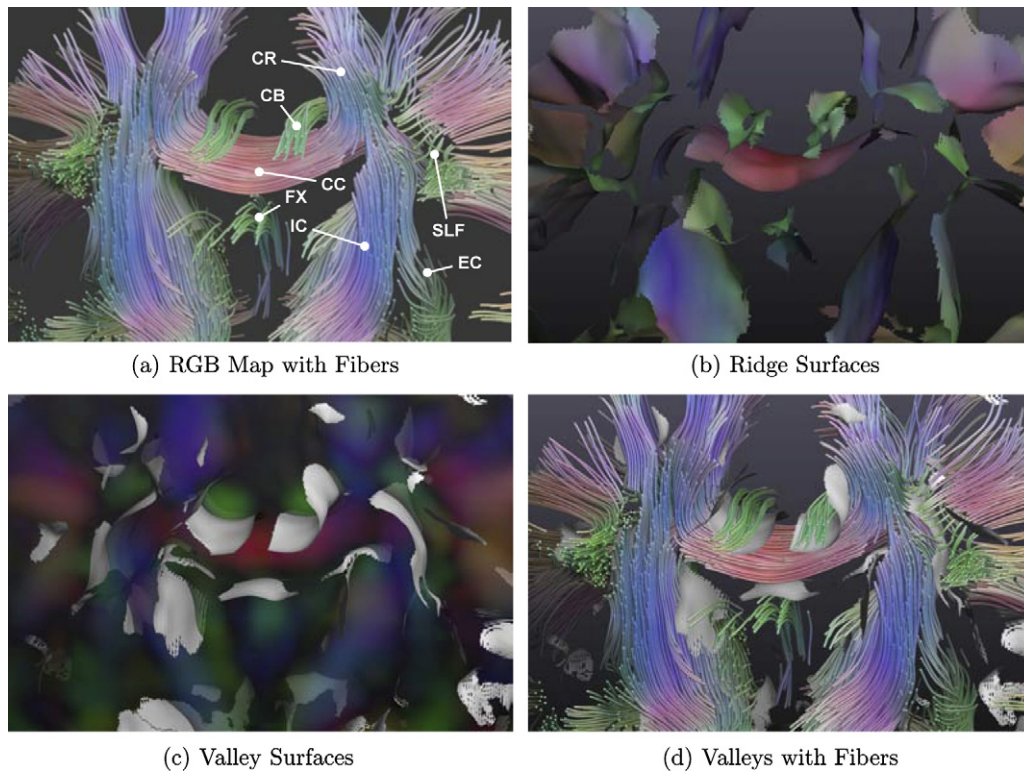


Fig. 4. Anisotropy creases near the corpus callosum. CC, corpus callosum; IC, internal capsule; CR, corona radiata; FX, fornix; CB, cingulum bundles; SFO, superior fronto-occipital fasciculus; SLF, superior longitudinal fasciculus.

The tract interfaces are delineated by the valley surfaces in Fig. 5c, which also includes for reference a translucent cutting plane with RGB coloring of the principal diffusivity

direction, as well as a view-aligned clipping plane to reveal the RGB color differences among the MCP, CST, and TPT. Fig. 5d illustrates how valley surfaces delineate major

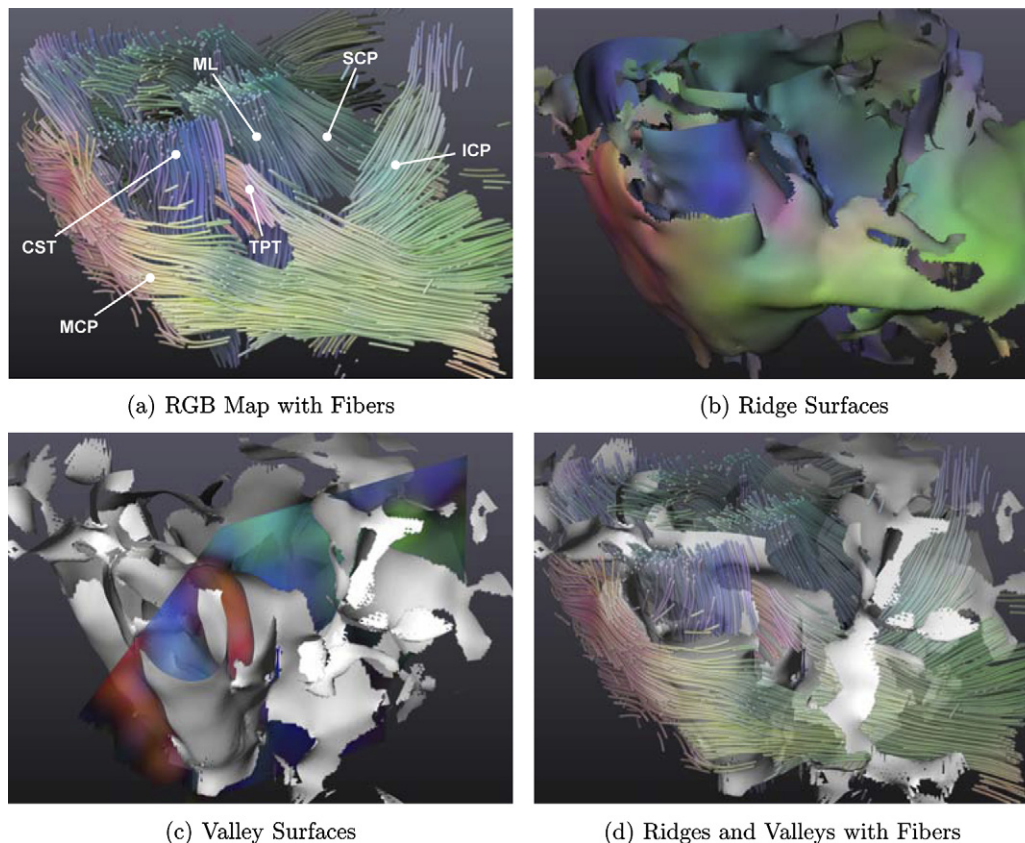


Fig. 5. Anisotropy creases in the brainstem.

fiber bundles, faintly visible as tractography results. In particular, valley surface patches are visible between MCP and CST, CST and TPT, TPT and ML, MCP and ICP, and ICP and SCP, all of which are locations where distinctly oriented fiber pathways pass near each other. The ridge and valley surface extractions each took 9 min.

Fig. 6 demonstrates the connected-component analysis mentioned in Section 3.1, which allows the main crease surface components to be extracted from the much larger collection of disjoint pieces. For these results and those in Fig. 7, the tensor datasets were down-sampled by a factor of two, to simplify the field to only its largest features. Ridge surface extraction on this dataset produced 742 surface connected-components (CCs), but Fig. 6 shows that the largest nine CCs capture nearly all the large fiber tracts visible in all CCs.

To demonstrate the repeatability of our method, Fig. 7 expands the results from Fig. 6 to include five other scans from the same database, all processed identically. The computation of these ridge surfaces took 6 min per dataset. In every case, the single largest connected-component contains a single surface representing the corpus callosum, as well as parts of other pathways, such as the corona radiata, and often the internal capsules. We are currently investigating why ridge surface patches corresponding to distinct fiber pathways can appear joined in our ridge surface analysis, which is likely related to the problem of kissing or crossing fiber tracts.

5. Discussion and future work

The preliminary results in this work suggest that anisotropy creases delineate the major white matter structure in DTI, and that analytically measured anisotropy derivatives (and an adaptation of marching cubes) can lead to high-quality triangulated models of crease surface geometry. In contrast to the combination of tractography and clustering algorithms, the invariance properties in the mathematical definition of anisotropy creases give them the attractive property of having very few parameters in their extraction. The main parameter is the scale of the Gaussian smoothing pre-process, since this puts a lower bound on the scale of the extracted features. Secondary parameters include the feature strength threshold (Section 2.3), the resolution of the crease triangulation grid, and the manner of selecting connected-components from the triangulation output (Section 3).

As mentioned in Section 1, our method is a *structural* analysis of features in DTI, and not the *connectivity* analysis that is a popular research focus. This has implications for the type of studies for which anisotropy creases may be applied in future work (described below), as our focus is on the over-all shape of the white matter pathways, rather than on their course. In particular, for the task of extracting a geometric model of the major white matter pathways, we accept the simplicity of the single tensor model, despite its well-known inability to represent fiber-

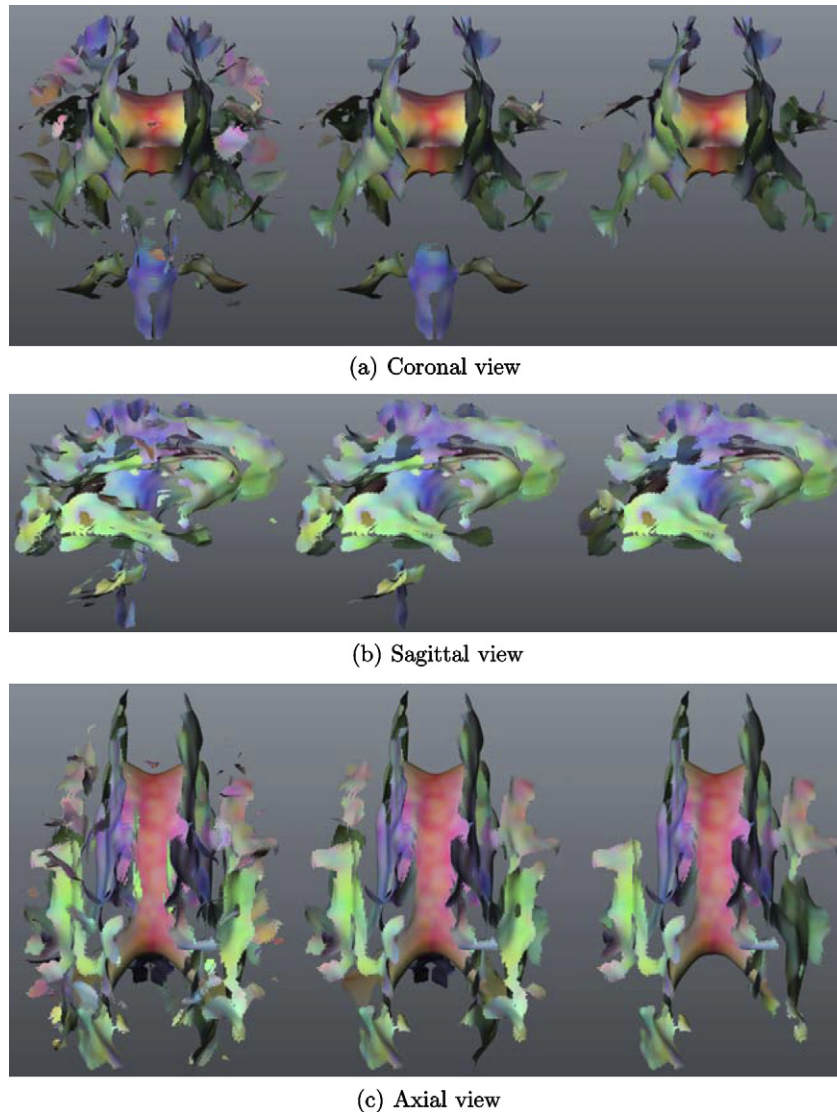


Fig. 6. Ridge surface extraction results from a single scan, showing different numbers of connected-components: all 742 (left), nine largest (middle), and single largest (right).

crossings and multiple fiber orientations (Alexander et al., 2002; Tuch et al., 2002), because it gives rise to a tractable analysis of the differential properties of anisotropy as parameterized by FA (Eq. (5)), and because for large portions of the major pathways (e.g., visualized in Fig. 4b), the single tensor model appears sufficient. Indeed, for the extraction of fiber pathway *interfaces* (Fig. 4c), we embrace the fact that the partial voluming of distinctly oriented pathways gives rise to artifactual planar anisotropy by component-wise interpolation (Alexander et al., 2001), which leads to lower FA values (Fig. 2b), which in turn enables FA valley surfaces to geometrically isolate the interfaces (Figs. 2c and 4c). On the other hand, for future work one could also consider measuring the differential properties of continuous maps of non-tensor or higher-order anisotropy measures (Özarslan et al., 2005; Descoteaux et al., 2006), which could possibly generate geometric models of areas of fiber-crossings in particular, or highlight

where our current FA-based analysis could be most misleading.

The continuous tensor field reconstruction method we use (Aldroubi and Basser, 1999; Pajevic et al., 2002) is “Euclidean” in that it implicitly considers diffusion tensors as elements of a vector space, even though this neglects the strictly positive-definite nature of diffusion. The DTI literature provides a precedent for this simplifying assumption in other contexts as well (Basser et al., 2000; Basser and Pajevic, 2003; Basser and Pajevic, 2007). In a different line of recent work, however, tensors are located on a Riemannian manifold that effectively creates an infinite distance between valid tensors and those with zero determinant (Pennec, 2004; Fletcher and Joshi, 2004; Batchelor et al., 2005; Lenglet et al., 2006), and the Log-Euclidean methods provide computationally efficient approximations (Arsigny et al., 2006; Fillard et al., 2006). The relative strengths of these two approaches (Euclidean

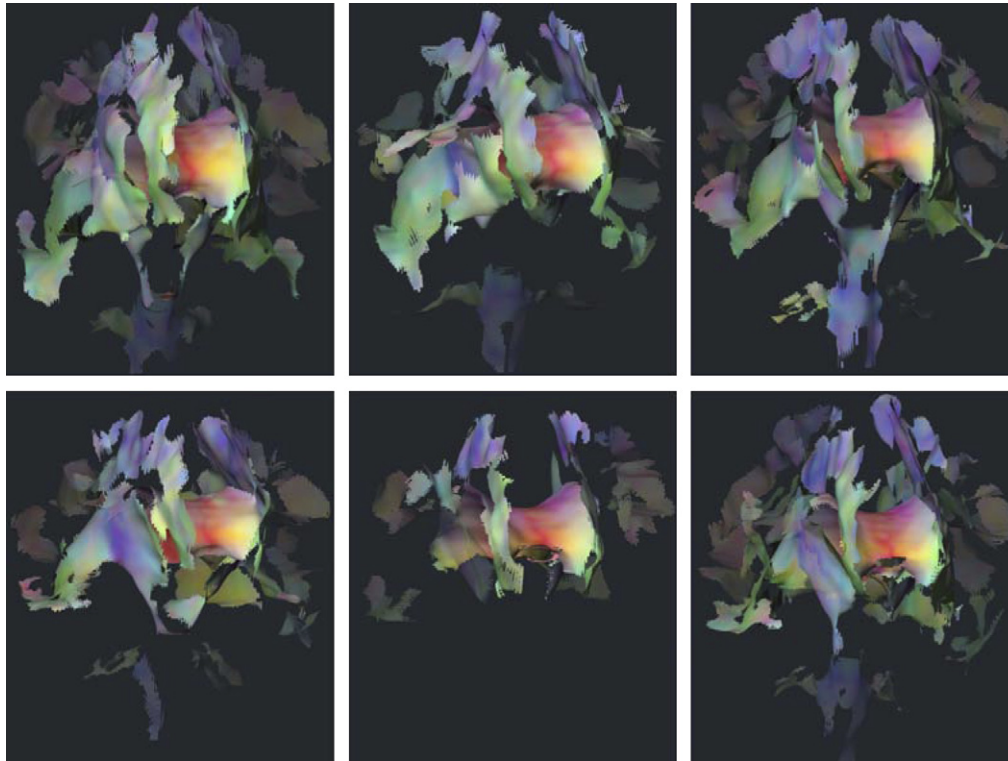


Fig. 7. Ridge surface extraction results from six scans, viewed from an anterior (and slightly right) viewpoint, showing largest connected-component (solid) and next eight largest CCs (translucent).

versus Riemannian) is an ongoing issue that we do not intend to resolve here, although some basic points bear consideration. First, it is possible to define tensor field derivatives on a Riemannian manifold (Lenglet et al., 2006), from which anisotropy derivatives could also be computed. Thus, in principal anisotropy creases could be extracted entirely within a Riemannian framework, though at an increased computation cost. On the other hand, the distinction between the Euclidean and Riemannian approaches may be viewed more simply as a difference in choosing whether to enforce positive-definiteness solely at the data acquisition stage (Euclidean), or also at the analysis stage (Riemannian). We view the enforcement of this constraint as orthogonal to the task of analyzing the differential structure of anisotropy, especially since FA is defined without regard to positive-definiteness (which has apparently not hindered its scientific utility).

Our ongoing algorithmic work is focused on geometric extraction of FA ridge *lines* (for example through the cingulum bundles), and then comparing the FA ridge lines to individual fiber tracts. There are also theoretical questions remaining about the differential structure of FA. Given the scale of the Gaussian smoothing pre-process, and the properties of the cubic reconstruction kernel, we would like to determine an upper bound on the resolution of the surface triangulation grid (relative to the original tensor samples) that is guaranteed to find all anisotropy creases. In the case of valleys in FA, we would like to quantify the relationship between strength

and location of the valley surface, and the linear anisotropy levels and orientation of the two neighboring regions.

Developing applications of anisotropy crease features is the main focus of future work. Following the example of TBSS (Smith et al., 2006; Rouw and Scholte, 2007), we are interested in using anisotropy crease features as manifolds onto which neuroanatomic variables can be projected for the purposes of comparison and study. While TBSS generates a discretized FA ridge surface map, we are curious whether having true codimension-one surfaces, for both ridges and valleys, extracted from individual cases instead of a group registration result, can increase the statistical power of analysis based on anisotropy creases. The second main application area for future work is in providing fiducial markers to drive non-rigid registration of DTI. Related work is described in Goodlett et al. (2006), although here too the results are in the form of discrete images rather than continuous surfaces. Using valley surfaces of FA to explicitly model the interfaces between adjacent but orthogonal fiber tracts may usefully guide non-rigid registration of tensor fields for group studies. Slight mis-registration of these configurations could lead to comparison of tensor values within entirely separate pathways. In addition, just as shape analysis of segmented structures from scalar MRI is an active area of medical image research (e.g., Styner et al. (2004)), anisotropy creases from DTI may also support informative shape analysis.

Finally, to extract true image *cores*, crease detection must work simultaneously across image scales (Furst et al., 1996; Lindeberg, 1998). This will incur greater computational cost, and perhaps algorithmic complexity, but we are investigating methods to limit the computation to regions around crease features (generalizing the existing strategy of skipping voxels with low feature strength). We believe that incorporating scale-space analysis into our crease feature extraction may give the method better noise robustness, because feature strength would be stronger at the larger scales where noise is smoothed out.

Acknowledgements

This work supported by NIH Grants NIBIB T32-EB002177, U41 RR019703 (IGT), NCRP P41-RR13218 (NAC) and P41-RR12553-07 (CIBC), R01-MH050740, and R01-MH074794. DWI data courtesy of Dr. Susumu Mori, Johns Hopkins University, supported by NIH R01-AG20012-01 and P41-RR15241-01A1.

Appendix A. Hessian of Fractional Anisotropy

The Hessian of fractional anisotropy (FA) is determined by differentiating Eqs. (5)–(7). The differential operator ∇ produces a column vector, and $\mathbf{H} = \nabla\nabla^T$ produces the Hessian matrix of second partial derivatives.

$$\mathbf{H}(\text{FA}) = \frac{\nabla J_2 \nabla^T J_4 - \nabla J_4 \nabla^T J_2 + J_2 \mathbf{H}(J_4) - J_4 \mathbf{H}(J_2)}{2J_4^2 \text{FA}} - \frac{(2J_4 \nabla J_4 \text{FA} + J_4^2 \nabla \text{FA})(J_2 \nabla^T J_4 - J_4 \nabla^T J_2)}{2(J_4^2 \text{FA})^2} \quad (\text{A.1})$$

$$\begin{aligned} \mathbf{H}(J_2) = & (\nabla D_{yy} + \nabla D_{zz}) \nabla^T D_{xx} + (D_{yy} + D_{zz}) \mathbf{H}(D_{xx}) \\ & + (\nabla D_{xx} + \nabla D_{zz}) \nabla^T D_{yy} + (D_{xx} \\ & + D_{zz}) \mathbf{H}(D_{yy}) + (\nabla D_{xx} + \nabla D_{yy}) \nabla^T D_{zz} \\ & + (D_{xx} + D_{yy}) \mathbf{H}(D_{zz}) - 2(\nabla D_{xy} \nabla^T D_{xy} \\ & + D_{xy} \mathbf{H}(D_{xy}) + \nabla D_{xz} \nabla^T D_{xz} + D_{xz} \mathbf{H}(D_{xz}) \\ & + \nabla D_{yz} \nabla^T D_{yz} + D_{yz} \mathbf{H}(D_{yz})) \end{aligned} \quad (\text{A.2})$$

$$\begin{aligned} \mathbf{H}(J_4) = & 2(\nabla D_{xx} \nabla^T D_{xx} + D_{xx} \mathbf{H}(D_{xx}) + \nabla D_{yy} \nabla^T D_{yy} \\ & + D_{yy} \mathbf{H}(D_{yy}) + \nabla D_{zz} \nabla^T D_{zz} + D_{zz} \mathbf{H}(D_{zz})) \\ & + 4(\nabla D_{xy} \nabla^T D_{xy} + D_{xy} \mathbf{H}(D_{xy}) \\ & + \nabla D_{xz} \nabla^T D_{xz} + D_{xz} \mathbf{H}(D_{xz}) + \nabla D_{yz} \nabla^T D_{yz} \\ & + D_{yz} \mathbf{H}(D_{yz})) \end{aligned} \quad (\text{A.3})$$

References

Aldroubi, A., Basser, P., 1999. Reconstruction of vector and tensor fields from sampled discrete data. *Contemporary Mathematics* 247, 1–15.
 Alexander, A., Hasan, K., Lazar, M., Tsuruda, J., Parker, D., 2001. Analysis of partial volume effects in diffusion-tensor MRI. *Magnetic Resonance in Medicine* 45, 770–780.

Alexander, D., Barker, G., Arridge, S., 2002. Detection and modeling of non-gaussian apparent diffusion coefficients profiles in human brain data. *Magnetic Resonance in Medicine* 48, 331–340.
 Arsigny, V., Fillard, P., Pennec, X., Ayache, N., 2006. Log-Euclidean metrics for fast and simple calculus on diffusion tensors. *Magnetic Resonance in Medicine* 56 (2), 411–421.
 Basser, P., 1995. Inferring microstructural features and the physiological state of tissues from diffusion-weighted images. *Nuclear Magnetic Resonance in Biomedicine* 8, 333–344.
 Basser, P., Jones, D., 2002. Diffusion-tensor MRI: theory, experimental design and data analysis – a technical review. *Nuclear Magnetic Resonance in Biomedicine* 15, 456–467.
 Basser, P.J., Pajavic, S., 2003. A normal distribution for tensor-valued random variables: applications to diffusion tensor MRI. *IEEE Transactions on Medical Imaging* 22 (7), 785–794.
 Basser, P.J., Pajevic, S., 2007. Spectral decomposition of a 4th-order covariance tensor: applications to diffusion tensor MRI. *Signal Processing* 87, 220–236.
 Basser, P.J., Pierpaoli, C., 1996. Microstructural and physiological features of tissues elucidated by quantitative-diffusion-tensor MRI. *Journal of Magnetic Resonance, Series B* 111, 209–219.
 Basser, P., Mattiello, J., LeBihan, D., 1994. MR diffusion tensor spectroscopy and imaging. *Biophysics Journal* 66 (1), 259–267.
 Basser, P.J., Pajevic, S., Pierpaoli, C., Duda, J., Aldroubi, A., 2000. In vivo fiber tractography using DT-MRI data. *Magnetic Resonance in Medicine* 44, 625–632.
 Batchelor, P.G., Moakher, M., Atkinson, D., Calamante, F., Connelly, A., 2005. A rigorous framework for diffusion tensor calculus. *Magnetic Resonance in Medicine* 53 (1), 221–225.
 Beaulieu, C., 2002. The basis of anisotropic water diffusion in the nervous system – a technical review. *Nuclear Magnetic Resonance in Biomedicine* 15, 435–455.
 Bourne, D., Kendall, P., 1977. *Vector Analysis and Cartesian Tensors*, 2nd ed. Thomas Nelson and Sons, Ltd, Great Britain (Chapter 9).
 Corouge, I., Fletcher, P., Joshi, S., Gouttard, S., Gerig, G., 2006. Fiber tract-oriented statistics for quantitative diffusion tensor MRI analysis. *Medical Image Analysis* 10 (5), 786–798.
 de Saint-Venant, M., 1852. Surfaces à plus grande pente constituées sur des lignes courbes. *Bulletin de la Société Philomathématique de Paris*, 24–30.
 Descoteaux, M., Angelino, E., Fitzgibbons, S., Deriche, R., 2006. Apparent diffusion coefficients from high angular resolution diffusion imaging: estimation and applications. *Magnetic Resonance in Medicine* 56, 395–410.
 Dougherty, R.F., Ben-Shachar, M., Deutsch, G., Potanina, P., Bammer, R., Wandell, B.A., 2005. Occipital-callosal pathways in children: validation and atlas development. *Annals of the New York Academy of Sciences* 1064, 98–112.
 Eberly, D., Gardner, R., Morse, B., Pizer, S., 1994. Ridges for image analysis. *Journal of Mathematical Imaging and Vision* 4, 351–371.
 Fillard, P., Arsigny, V., Pennec, X., Ayache, N., 2006. Clinical DT-MRI estimation, smoothing and fiber tracking with Log-Euclidean metrics. In: *Proceedings of the Third IEEE International Symposium on Biomedical Imaging (ISBI 2006)*. LNCS, Arlington, Virginia, USA, pp. 786–789.
 Fletcher, P.T., Joshi, S., 2004. Principal geodesic analysis on symmetric spaces: statistics of diffusion tensors. *Proceedings ECCV 2004 Workshop on Computer Vision Approaches to Medical Image Analysis (CVAMIA)*. In: LNCS, vol. 31107. Springer-Verlag, pp. 87–98.
 Furst, J.D., Pizer, S.M., 2001. Marching ridges. In: *Proceedings of 2001 IASTED International Conference on Signal and Image Processing*, pp. 22–26.
 Furst, J.D., Pizer, S.M., Eberly, D.H., June 1996. Marching cores: a method for extracting cores from 3D medical images. In: *Proceedings of IEEE Workshop on Mathematical Methods in Biomedical Image Analysis*, pp. 124–130.

- Gauch, J.M., Pizer, S.M., 1993. Multiresolution analysis of ridges and valleys in grey-scale images. *IEEE Transactions on Pattern Analysis and Machine Intelligence* 15 (6), 635–646.
- Gonzalez, R., Woods, R., 2002. *Digital Image Processing*, second ed. Addison-Wesley Publishing Company, Reading, MA.
- Goodlett, C., Davis, B., Jean, R., Gilmore, J.H., Gerig, G., 2006. Improved correspondence for DTI population studies via unbiased atlas building. In: *Ninth International Conference on Medical Image Computing and Computer-Assisted Intervention (MICCAI'06)*. Lecture Notes in Computer Science, vol. 4190. Copenhagen, Denmark, pp. 260–267.
- Haralick, R.M., 1983. Ridges and valleys on digital images. *Computer Vision, Graphics, and Image Processing* 22, 28–38.
- Kanaan, R.A.A., Kim, J.-S., Kaufmann, W.E., Pearlson, G.D., Barker, G.J., McGuire, P.K., 2005. Diffusion tensor imaging in schizophrenia. *Biological Psychiatry* 58, 921–929.
- Kindlmann, G., Tricoche, X., Westin, C.-F., 2006. Anisotropy creases delineate white matter structure in diffusion tensor MRI. In: *Proceedings MICCAI 2006*. Lecture Notes in Computer Science, vol. 4190. Copenhagen, Denmark, pp. 126–133.
- Klingberg, T., Hedehus, M., Temple, E., Salz, T., Gabrielli, J.D.E., Moseley, M.E., Poldrack, R.A., 2000. Microstructure of temporoparietal white matter as a basis for reading ability: evidence from diffusion tensor magnetic resonance imaging. *Neuron* 25, 493–500.
- Kubicki, M., Westin, C.-F., Maier, S., Mamata, H., Frumin, M., Ernst-Hirschfeld, H., Kikinis, R., Jolesz, F., McCarley, R., Shenton, M., 2003. Cingulate fasciculus integrity disruption in schizophrenia: a magnetic resonance diffusion tensor imaging study. *Biological Psychiatry* 54, 1171–1180.
- Lenglet, C., Rousson, M., Deriche, R., 2006. DTI segmentation by statistical surface evolution. *IEEE Transactions on Medical Imaging* 25, 685–700.
- Lindeberg, T., 1998. Edge detection and ridge detection with automatic scale selection. *International Journal of Computer Vision* 30 (2), 77–116.
- Lorensen, W.E., Cline, H.E., 1987. Marching cubes: a high resolution 3D surface construction algorithm. *Computer Graphics* 21 (4), 163–169.
- Marsden, J., Tromba, A., 1996. *Vector Calculus*. W.H. Freeman and Company, New York.
- Maxwell, J., 1870. On hills and dales. *The London, Edinburgh and Dublin Philosophical Magazine and Journal of Science* 40 (269), 421–425.
- Moberts, B., Vilanova, A., van Wijk, J.J., 2005. Evaluation of fiber clustering methods for diffusion tensor imaging. In: *Proceedings IEEE Visualization 2005*, pp. 65–72.
- Mori, S., Wakana, S., Nagae-Poetscher, L., Zijl, P.V., 2005. *MRI Atlas of Human White Matter*. Elsevier.
- Morse, B.S., 1994. *Computation of object cores from grey-level images*. Ph.D. thesis, University of North Carolina at Chapel Hill, Chapel Hill, NC.
- O'Donnell, L., Grimson, W., Westin, C.-F., 2004. Interface detection in diffusion tensor MRI. In: *Proceedings MICCAI 2004*, pp. 360–367.
- O'Donnell, L., Kubicki, M., Shenton, M.E., Dreusicke, M., Grimson, W.E.L., Westin, C.-F., 2006. A method for clustering white matter fiber tracts. *American Journal of Neuroradiology* 27, 1032–1036.
- Özarslan, E., Vemuri, B.C., Mareci, T.H., 2005. Generalized scalar measures for diffusion MRI using trace, variance, and entropy. *Magnetic Resonance in Medicine* 53, 866–876.
- Pajevic, S., Pierpaoli, C., 1999. Color schemes to represent the orientation of anisotropic tissues from diffusion tensor data: application to white matter fiber tract mapping in the human brain. *Magnetic Resonance in Medicine* 42 (3), 526–540.
- Pajevic, S., Aldroubi, A., Basser, P., 2002. A continuous tensor field approximation of discrete DT-MRI data for extracting microstructural and architectural features of tissue. *Journal of Magnetic Resonance* 154, 85–100.
- Penec, X., 2004. Probabilities and statistics on riemannian manifolds: a geometric approach. Tech. Rep. 5093, INRIA, Sophia Antipolis.
- Pierpaoli, C., Jezzard, P., Basser, P., Barnett, A., DiChiro, G., 1996. Diffusion tensor MR imaging of the human brain. *Radiology* 201 (3), 637–648.
- Rouw, R., Scholte, H.S., 2007. Increased structural connectivity in grapheme-color synesthesia. *Nature Neuroscience* 10, 792–797.
- Salamon, N., Sicotte, N., Alger, J., Shattuck, D., Perlman, S., Sinha, U., Schultze-Haak, H., Salamon, G., 2005. Analysis of the brain-stem white-matter tracts with diffusion tensor imaging. *Neuroradiology* 47 (12), 895–902.
- Salat, D.H., Tuch, D.S., Hevelone, N.D., Fischl, B., Corkin, S., Rosas, H.D., Dale, A.M., 2005. Age-related changes in prefrontal white matter measured by diffusion tensor imaging. *Annals of the New York Academy of Sciences* 1064, 37–49.
- Shreiner, D., Woo, M., Neider, J., Davis, T., 2004. *OpenGL Programming Guide*, 4th ed. Addison-Wesley.
- Smith, S.M., Jenkinson, M., Johansen-Berg, H., Rueckert, D., Nichols, T.E., Mackay, C.E., Watkins, K.E., Ciccarelli, O., Cader, M.Z., Matthews, P.M., Behrens, T.E.J., 2006. Tract-based spatial statistics: voxelwise analysis of multi-subject diffusion data. *NeuroImage* 31, 1487–1505.
- Styner, M., Lieberman, J.A., Pantazis, D., Gerig, G., 2004. Boundary and medial shape analysis of the hippocampus in schizophrenia. *Medical Image Analysis* 8 (3), 197–203.
- ter Haar Romeny, B.M., 2003. *Front-end vision and multi-scale image analysis*. In: *Computational Imaging and Vision*, vol. 27. Kluwer Academic Publishers, Dordrecht, The Netherlands.
- Tuch, D.S., Reese, T.G., Wiegell, M.R., Makris, N., Belliveau, J.W., Wedeen, V.J., 2002. High angular resolution diffusion imaging reveals intravoxel white matter fiber heterogeneity. *Magnetic Resonance in Medicine* 48, 577–582.
- Tuch, D.S., Salat, D.H., Wisco, J.J., Zaleta, A.K., Hevelone, N.D., Rosas, H.D., 2005. Choice reaction time performance correlates with diffusion anisotropy in white matter pathways supporting visuospatial attention. *Proceedings of the National Academy of Sciences* 102 (34), 12212–12217.
- Zhang, S., Correia, S., Tate, D.F., Laidlaw, D.H., 2006. Correlating DTI fiber clusters with white-matter anatomy. In: *Proceedings International Society for Magnetic Resonance in Medicine (ISMRM)*, p. 442.